

CRISPR-Cas9 screening identifies KRAS-induced COX-2 as a driver of immunotherapy resistance in lung cancer

Jesse Boumelha¹, Andrea de Castro¹, Nourdine Bah², Hongui Cha^{3,4}, Sophie de Carné Trécesson¹, Sareena Rana¹, Mona Tomaschko¹, Panayiotis Anastasiou¹, Edurne Mugarza¹, Christopher Moore¹, Robert Goldstone², Phil East², Kevin Litchfield⁴, Se-Hoon Lee³, Miriam Molina-Arcas¹, Julian Downward¹.

¹ Oncogene Biology Laboratory, ² Bioinformatics and Biostatistics, Francis Crick Institute, 1 Midland Road, London NW1 1AT, UK

³ Division of Hematology-Oncology, Department of Medicine, Samsung Medical Center, Sungkyunkwan University School of Medicine, Seoul 06351, Republic of Korea

⁴ Cancer Research UK Lung Cancer Centre of Excellence, University College London Cancer Institute, London, UK

Running Title: KRAS induces COX-2 to drive immune evasion in lung cancer

Corresponding Authors: Julian Downward, Francis Crick Institute, 1 Midland Road, London NW1 1AT, United Kingdom. Email: julian.downward@crick.ac.uk; and Miriam Molina, Francis Crick Institute, 1 Midland Road, London NW1 1AT, United Kingdom. Email: miriam.molina@crick.ac.uk

Conflict of interest statement: J.D. has acted as a consultant for AstraZeneca, Jubilant, Theras, Roche and Vividion and has funded research agreements with Bristol Myers Squibb, Revolution Medicines and AstraZeneca. S.C.T has acted as a consultant for Revolution Medicines. K.L. has a patent on indel burden and CPI response pending and speaker fees from Roche tissue diagnostics, research funding from CRUK TDL/Ono/LifeArc alliance, and a consulting role with Monopteros Therapeutics. The other authors declare that they have no competing interests.

ABSTRACT

Oncogenic KRAS impairs anti-tumor immune responses. As effective strategies to combine KRAS inhibitors and immunotherapies have so far proven elusive, a better understanding of how oncogenic KRAS drives immune evasion is needed to identify approaches that could sensitize KRAS-mutant lung cancer to immunotherapy. *In vivo* CRISPR-Cas9 screening in an immunogenic murine lung cancer model identified mechanisms by which oncogenic KRAS promotes immune evasion, most notably via upregulation of immunosuppressive cyclooxygenase-2 (COX-2) in cancer cells. Oncogenic KRAS potently induced COX-2 in both mouse and human lung cancer, which was suppressed using KRAS inhibitors. COX-2 acted via prostaglandin E2 (PGE₂) to promote resistance to immune checkpoint blockade (ICB) in lung adenocarcinoma. Targeting COX-2/PGE₂ remodeled the tumor microenvironment by inducing pro-inflammatory polarization of myeloid cells and influx of activated cytotoxic CD8⁺ T cells, which increased the efficacy of ICB. Restoration of COX-2 expression contributed to tumor relapse after prolonged KRAS inhibition. These results provide the rationale for testing COX-2/PGE₂ pathway inhibitors in combination with KRAS^{G12C} inhibition or ICB in patients with KRAS-mutant lung cancer.

Statement of significance:

COX-2 signaling via prostaglandin E2 is a major mediator of immune evasion driven by oncogenic KRAS that promotes immunotherapy and KRAS-targeted therapy resistance, suggesting effective combination treatments for KRAS-mutant lung cancer.

INTRODUCTION

Despite improvements in systemic therapies, lung adenocarcinoma (LUAD) remains the most common cause of cancer-related deaths worldwide (1). Immune checkpoint blockade (ICB), which can reinvigorate anti-tumor immunity, has shown remarkable clinical success in multiple cancer types (2), including LUAD (3), achieving durable responses in a subset of patients. Monoclonal antibodies targeting the immunosuppressive PD-L1/PD-1 axis have become standard of care for LUAD patients, either as a monotherapy (4) or in combination with chemotherapy (5). However, only a fraction of patients benefits from ICB highlighting the need for combination strategies that will broaden responses to current immunotherapies. Recent clinical efforts, such as the SKYSCRAPER-01 trial combining PD-L1 blockade with an anti-TIGIT antibody, have failed to lead to improved responses in lung cancer and there is a need to better understand mechanisms of immune evasion in order to design rational combination strategies that are more likely to provide clinical benefit.

Mutations in the oncogene KRAS drive tumorigenesis in 30% of LUAD cases (6). However, the development of inhibitors that directly target KRAS has been notoriously challenging (7). A major breakthrough was achieved with the recent development of mutant-specific KRAS^{G12C} inhibitors (8) which covalently bind to the novel cysteine residue present in nearly half of all KRAS-mutant LUAD patients (9). This has led to the approval of Amgen's clinical compound sotorasib for the treatment of locally advanced or metastatic KRAS^{G12C}-mutant lung cancer (10). Whilst these drugs have mild toxicities and achieve clinical responses in a substantial proportion of patients, as with other targeted therapies, responses are often short-lived as resistance inevitably arises (11).

Accumulating evidence suggests that oncogenic signaling extends beyond the tumor cell compartment and engages with the host stromal and immune compartments. Consequently, oncogenic drivers have been shown to play dominant roles in shaping the tumor immune landscape of different cancers and inhibiting anti-tumor immune responses (12). Analysis of clinical samples has demonstrated that KRAS mutations are associated with an immunosuppressive tumor microenvironment (TME) (13) and preclinical studies have identified a number of mechanisms by which oncogenic KRAS

can drive immune evasion including promoting the expression of numerous immunosuppressive myeloid chemoattractants (14,15) and immune checkpoint ligands (16). Together these observations provide a rational basis for combining KRAS inhibitors with ICB and numerous preclinical studies have demonstrated that this combination leads to improved therapeutic responses, at least in immunogenic models (15,17,18). However, recent reports of the CODEBREAK 100/101 clinical trial evaluation of sotorasib in combination with anti-PD-L1/PD-1 antibodies have shown serious toxicities (19,20), casting doubt on the viability of this combination. As an alternative approach, a greater understanding of how oncogenic KRAS drives immune evasion may identify novel immunotherapy combination strategies that could improve outcomes for KRAS-mutant lung cancer patients.

Pooled CRISPR screens have been increasingly used to uncover tumor-intrinsic determinants of anti-tumor immunity, identifying numerous genes that either promote sensitivity or resistance to immune control (21–25). We recently developed a novel immunogenic model of KRAS-mutant lung cancer allowing for the preclinical study of tumor-immune interactions (17). Here we carry out a pooled *in vivo* CRISPR screen in this novel model to interrogate the role of 240 KRAS-regulated genes in controlling anti-tumor immunity. This identified several genes that increased sensitivity or resistance to anti-tumor immune responses. Among these, the prostaglandin synthase cyclooxygenase-2 (COX-2), responsible for synthesis of the immunosuppressive molecule prostaglandin E₂ (PGE₂), was identified as a major driver of immune evasion and resistance to immunotherapy in both mouse and human lung cancer. Targeting of the COX-2/PGE₂ axis improved the response of KRAS-mutant lung tumors to anti-PD-1 therapy by inducing pro-inflammatory polarisation of myeloid cells and enhancing T cell infiltration and activation. Importantly, oncogenic KRAS signaling was a strong driver of the COX-2/PGE₂ signaling axis in both mouse and human LUAD and COX-2 inhibition delayed tumor relapse after KRAS^{G12C} inhibition.

MATERIALS AND METHODS

In vivo tumor studies

All animal studies were approved by the ethics committee of the Francis Crick Institute and conducted according to local guidelines and UK Home Office regulations under the Animals Scientific Procedures Act 1986 (ASPA).

All transplantation animal experiments were carried out using 8-12-week C57BL/6J mice. For orthotopic experiments, mice were injected intravenously into the tail-vein with 1.5×10^5 KPAR or KPAR^{G12C} cells. Mice were euthanized when mice displayed signs of ill health or exceeded 15% weight loss. For subcutaneous experiments, 1×10^6 3LL Δ NRAS cells were injected subcutaneously into the left flank (1:1 mix with Matrigel). Tumors were measured twice weekly using callipers and volume calculated using the formula $0.5 \times \text{length} \times \text{width}^2$. Mice were euthanized when the average tumor dimension exceeded 1.5 cm. *Kras*^{LSL-G12D/+}; *Trp53*^{fl/fl} mice (KP) were sourced from the Mouse Models of Human Cancer Consortium and maintained on a pure C57BL/6 background. Tumors were induced by intratracheal intubation of 1×10^6 adenovirus expressing Cre recombinase.

For antibody treatments, 200 μ g anti-PD-1 (clone RMP1-14, BioXcell, AB_2927529) or the respective IgG control (AB_1107769), were administered via intraperitoneal injection twice weekly for a maximum of three weeks. For drug treatments, 50 mg/kg MRTX849 (MedChem Express), 1.3 mg/kg trametinib (LC laboratories), 16.6 mg/kg linsitinib (Astellas), 1.6 mg/kg everolimus (LC laboratories), 30 mg/kg celecoxib (LC laboratories), 100 mg/kg TPST-1495 (kindly provided by Tempest Therapeutics) or their respective vehicles were administered daily or twice daily via oral gavage for the stated duration. MRTX849 was prepared in 10% Captisol diluted in 50mM citrate buffer (pH 5.0), trametinib, everolimus and linsitinib in 0.5% methylcellulose/0.2% Tween 80, celecoxib in a mixture of 10% DMSO, 50% polyethylene glycol 400, and 40% water and TPST-1495 in 0.5% methylcellulose. For orthotopic experiments involving targeted therapies, mice were randomized into groups and treatments initiated once lung tumors reached an average volume of 1.5 mm^3 as detected by micro-CT.

For depletion experiments, mice received 200µg anti-CD8 (2.43, AB_1125541) and/or 200µg anti-NK1.1 (PK136, AB_1107737) via intraperitoneal injection one and three days before tumor cell transplantation followed by once weekly for the duration of the experiment. Depletion was confirmed by flow cytometry using anti-CD49b-AF488 (DX5, Biolegend, AB_492879) and anti-Nkp46-BV421 (29A1.4, Biolegend, AB_2737837), for NK cells and anti-CD8-PE (53-6.7, BD Biosciences, AB_394571) for CD8⁺ T cells.

sgRNA library generation

sgRNAs were designed to target upstream of the first functional domain of each gene. This was identified for each gene using the CDS of the principal isoform (APPRIS database) for each transcript and protein domain annotation from the Pfam database. The top five ranked sgRNAs, based on on-target and off-target activity, were chosen. Some genes could only be targeted by four sgRNAs due to their short length. 1,191 sgRNAs, targeting 240 genes, were designed using the GPP sgRNA designer (<http://portals.broadinstitute.org/gpp/public/analysis-tools/sgrna-design>). 50 non-targeting sgRNAs were also used from the mouse GeCKOv2 library. Annealed oligonucleotides corresponding to each sgRNA were combined into 10 different pools, each containing 125 sgRNAs and 5 non-targeting controls, and cloned into a lentiviral vector (pLenti_BSD_sgRNA). Lentiviral libraries were produced using each of the 10 pools and stored at -80°C. The sgRNA sequences used in the library are given in Supplementary Table 1.

***In vivo* CRISPR screening**

1x10⁶ KPAR iCas9 cells were infected with each of the 10 lentivirus pools at an MOI of 0.3. 24h after infection, cells were selected in blasticidin (10 µg/ml, InvivoGen) for 4 days. Selected were subsequently expanded *in vitro* and Cas9 induced by doxycycline (1 µg/ml, Sigma) for 6 days. Cells were then changed into normal media for 2 days before being orthotopically transplanted into mice. 1.25x10⁵ library-transduced cells were injected intravenously into the tail-vein of wild-type C57BL/6J mice and *Rag2*^{-/-}; *Il2rg*^{-/-} mice. In parallel, library-transduced cells were cultured *in vitro* at a library

representation of >2000x for the same time period as the *in vivo* experiment. Tumors were harvested 3 weeks after transplantation and genomic DNA was extracted from tumors using the Gentra Puregene DNA Extraction kit (QIAGEN).

Two-step PCR of genomic DNA was performed to amplify the sgRNA sequences and attach sequencing adaptors required for Illumina sequencing. sgRNA representation in each sample was measured by sequencing amplicons using an Illumina NextSeq 500. Data analysis was performed by the bioinformatics facility at the Francis Crick Institute. Briefly, reads were initially assigned to each sample using the indexed barcodes and then aligned to one of the possible sgRNAs in the library. Reads were normalized to total read counts per sample using MAGeCK and log₂-fold change between groups calculated. Guides with less than 15,000 reads at the time of library transduction were removed from the analysis.

Cell lines

KPAR, KPAR^{G12C}, 3LL ΔNRAS were generated as previously described (17,26). CT26^{G12C} were kindly provided by Mirati Therapeutics (27). NCI-H23 (CVCL_1547), NCI-H358 (CVCL_1559), NCI-H1792 (CVCL_1495), NCI-H2030 (CVCL_1517) and A549 (CVCL_0023) were obtained from the Francis Crick Institute Cell Services Facility. Cell lines were cultured in DMEM or RPMI supplemented with fetal bovine serum (10%), L-glutamine (2mM), penicillin (100 units/mL) and streptomycin (100 µg/mL). Clonal cell lines were derived by single-cell dilution into 96 well plates in DMEM-F12 supplemented with GlutaMAX, FBS (10%), hydrocortisone (1µM), EGF (20 ng/ml) and IGF (50ng/ml). Cell lines were routinely tested for mycoplasma infection and were authenticated by short-tandem repeat (STR) DNA profiling by the Francis Crick Institute Cell Services facility. For *in vitro* growth experiments, 2x10⁴ cells were plated in 96-well plates and cell confluency was monitored every 3h for 5 days using an IncuCyte Zoom system (Essen Biosciences).

In vitro treatments

Drugs or cytokines were added in fresh media 24h after seeding cells at stated concentrations and samples were obtained at indicated time points.

Flow cytometry

Mouse tumors were cut into small pieces and incubated with collagenase type I (1 mg/ml; ThermoFisher) and DNase I (50 U/ml; Life Technologies) in HBSS for 45 min at 37°C. Cells were filtered through 70 µm strainers (Falcon) and red blood cells were lysed using ACK buffer (Life Technologies). Samples were stained with fixable viability dye eFluor870 (BD Horizon) for 30 min and blocked with CD16/32 antibody (Biolegend) for 10 min before fluorescently-labelled antibody staining of surface markers (see Supplementary Table 2, Supplementary Fig. 5A-B). Intracellular staining was then performed after fixation using the Fixation/Permeabilization kit (eBioscience) according to the manufacturer's instructions. Samples were resuspended in FACS buffer and analysed using a BD Symphony flow cytometer. Data was analysed using FlowJo (Tree Star).

For FACS analysis *in vitro*, cells were trypsinized, washed with FACS buffer and stained with the following antibodies: anti-IFN γ R- β -chain-PE (MOB-47, BioLegend, AB_313560), anti-H2Db-PE (KH95, BioLegend, AB_313512) or anti-PD-L1-PE-Cy7 (10F.9G2, BioLegend, AB_10643573).

Immunohistochemistry

Tumor-bearing lungs were fixed in 10% NBF for 24h and transferred to 70% ethanol. Fixed lungs were processed into paraffin-embedded blocks. Tissue sections were stained with haematoxylin and eosin, using the automated TissueTek Prisma slide stainer. For immunohistochemistry staining, sections were boiled in sodium citrate buffer (pH 6.0) for 15 min and incubated with the following antibodies for 1h: anti-CD8 (4SM15, Thermo Scientific, AB_2572861), anti-NCR1 (EPR23097-35, Abcam, AB_2904203) and anti-Arg1 (D4E3M, Cell Signaling, AB_2800207). Primary antibodies were detected using biotinylated secondary antibodies and HRP/DAB detection. Slides were imaged using a Leica Zeiss AxioScan.Z1 slide scanner. Tumor-infiltrating immune cells were quantified using QuPath.

RT-qPCR

RNA was extracted from cell lines or frozen lung tumors using RNeasy kit (Qiagen). Single tumor nodules were plucked from tumor-bearing lungs. At least two tumors from at least three mice were included per group in each analysis. Frozen tumor samples were homogenized prior to RNA extraction using QIAshredder columns (Qiagen). cDNA was generated using the Maxima First Strand cDNA Synthesis Kit (Thermo Fisher Scientific) and qPCR performed using Applied Biosystems Fast SYBR Green reagents (Thermo Fisher Scientific). mRNA relative quantity was calculated using the $\Delta\Delta CT$ method and normalized to *Sdha*, *Hsp90* and *Tbp*. For heatmap visualisation, relative mRNA expression for each gene was log-transformed and median-normalized. Hierarchical clustering of gene expression data was carried out with the Euclidian distance metric using Morpheus (Broad Institute).

ELISA assay

Cells were treated as indicated for 48h. Conditioned media was collected and PGE₂ concentration determined using the Prostaglandin E2 parameter assay kit (R&D), as per manufacturer's instructions.

ELISPOT assay

1×10^5 CD8⁺ T cells were isolated from spleens of tumor-bearing mice using the EasyStep Mouse CD8a Positive selection Kit (Stemcell Technologies) and pulsed with 1 μ M of the eMLV *env* MHC-I restricted peptide (KSPWFTTL). Cells were stimulated for 24h in anti-mouse IFN γ -coated ELISPOT plates (BD Bioscience) and developed according to manufacturer's instructions. Spots were quantified using a CTL S6 machine.

siRNA experiments

Cells were seeded in a 6-well plate and reverse-transfected with 50nM siGENOME siRNA pools targeting mouse *Myc* (Dharmacon) using DharmaFECT 4 transfection reagent (Dharmacon) according to the manufacturer's instructions. 24h after transfection, cells were treated for 24h with trametinib (10nM). Control cells were

mock-transfected (no siRNA) or transfected with siGENOME RISC-free control siRNA (Dharmacon).

MicroCT imaging

Mice were anesthetized by inhalation of isoflurane and scanned using the Quantum GX2 micro-CT imaging system (Perkin Elmer). Serial lung images were reconstructed and tumor volumes subsequently analysed using Analyse (AnalyzeDirect) as previously described (28)

Western blotting

Cells were lysed using 10X Cell Lysis Buffer (Cell Signaling) supplemented with protease and phosphatase inhibitors (Roche). Protein concentration was determined using a BCA protein assay kit (Pierce) and 15-20µg of protein was separated on a 4-12% NuPAGE Bis-Tris gel (Life Technologies) followed by transfer to PVDF membranes. Proteins were detected by Western blotting using the following primary antibodies against: Flag (M2, Sigma, AB_262044), ERK1/2 (3A7, Cell Signaling, AB_10695739), p-ERK1/2 (Thr202/Tyr204) (9101, Cell Signaling, AB_331646), Myc (Y69, Abcam, AB_731658), STAT1 (9172, Cell Signaling, AB_2198300), p-STAT1 (T701) (58D6, Cell Signaling, AB_561284) STAT2 (D9J7L, Cell Signaling, AB_2799824) COX-2 (D5H5, Cell Signaling, AB_2571729), Vinculin (VIN-11-5, Sigma, AB_2877646) and β-Actin (8H10D10, Cell Signaling, AB_2242334). Primary antibodies were detected using HRP-conjugated secondary antibodies and visualized using standard film. Alternatively, membranes were incubated with secondary conjugates compatible with infrared detection at 700 nm and 800 nm and scanned using the Odyssey Infrared Imaging System (Odyssey, LICOR).

CRISPR-Cas9 knockout

Ptgs2^{-/-}, *Ifngr2*^{-/-} and *Etv4*^{-/-} KPAR cell lines were generated by transient transfection of a Cas9-sgRNA plasmid (pX459, Addgene) generated by standard molecular cloning techniques (see Supplementary Table 3 for sgRNA sequences). 3x10⁵ cells were seeded in a 6-well plate and transfected 24h later with 5 µg pX459

plasmid DNA using Lipofectamine 3000 (Thermo Scientific) according to the manufacturer's instructions. After 24h, cells were selected in puromycin (5 µg/ml, InvivoGen) for 48h. After selection, cells were single-cell cloned by single-cell dilution into 96 well plates. Knockout clones were identified by Western blot, ELISA or flow cytometry. *Edn1*^{-/-} KPAR cells were generated by infecting KPAR iCas9 cells with a pool of five different lentivirus each encoding a different sgRNA cloned into a lentiviral vector (pLenti_BSD_sgRNA). Cells were infected at a high multiplicity of infection (MOI) to maximise the number of lentivirus particles taken up by cells and increase the efficacy of editing. 24h after infection, cells were selected in blasticidin (10 µg/ml, InvivoGen) for 4 days and Cas9 induced by doxycycline (1 µg/ml, Sigma) for 6 days. As a negative control, cells were infected with a pool of five different lentivirus each encoding a different non-targeting sgRNA. sgRNAs were designed using the GPP sgRNA designer (<http://portals.broadinstitute.org/gpp/public/analysis-tools/sgrna-design>).

Stable cell lines, plasmids and lentivirus infection

For generation of the KPAR iCas9 cell line, KPAR cells were infected with the lentiviral vector pCW-Cas9 (Addgene) at a MOI of 0.3. 24h after infection, cells were selected in hygromycin (500 µg/ml, InvivoGen) for 7 days. Antibiotic-selected cells were single-cell cloned by single-cell dilution in 96 well plates. Clones with minimal expression of Cas9 in normal media and robust induction of Cas9 expression after 24h treatment with doxycycline (1 µg/ml, Sigma) were identified by Western blotting. Lentivirus particles were generated by co-transfection of HEK293T cells (CVCL_0063) with the lentiviral vector and packaging plasmids pCMV-VSV-G and pCMV-dR8.2. 48h after transfection, supernatant was collected, filtered through a 0.45µm filter and frozen at -80°C. Cells were infected with lentivirus particles by spinfection. Briefly, 1x10⁶ cells were plated in a 12-well plate along with 8 µg/ml polybrene (Millipore) and the specific volume of lentivirus depending on the MOI desired. Cells were centrifuged at 1000g for 2h at 33°C. 2ml of media was added after the spin and 16h later cells were trypsinized and plated into 6-well plates. 24h after spinfection cells were selected with appropriate antibiotic and subsequently expanded. MOI was calculated for each lentivirus batch by infecting target cells with different dilutions of lentivirus as previously described (29).

Bioinformatic analysis

The CCLE RNA-seq data were obtained from the CCLE repository hosted at The Broad (https://data.broadinstitute.org/ccle_legacy_data). We used the classification of RAS-low and RAS-high as previously described (30). All TCGA RNA-Seq gene-level read counts were downloaded using the TCGAbiolinks (TCGAbiolinks_2.8.4) package from Bioconductor (legacy=TRUE). Samples were classified in RAGs using RAS84, as previously shown (30). Raw counts for the TCGA LUAD, CCLE lung cell lines and LUAD ICB cohort were VST normalized using the varianceStabilizingTransformation function within DESeq2 (DESeq2_1.20.0) from Bioconductor.

The COX-IS score was calculated as the mean expression (vst estimate) of the COX-IS cancer-promoting genes (*VEGFA*, *CCL2*, *IL8*, *CXCL1*, *CXCL2*, *CSF3*, *IL6*, *IL1B* and *IL1A*) divided by the mean expression (vst estimate) of the COX-IS cancer-inhibitory genes (*CCL5*, *CXCL9*, *CXCL10*, *CXCL11*, *IL12A*, *IL12B*, *IFNG*, *CD8A*, *CD8B*, *GZMA*, *GZMB*, *EOMES*, *PRF1*, *STAT1* and *TBX21*), as previously described (31). The COX-IS was used to stratify ICB-treated LUAD patients into top 25% and bottom 25% quartiles and univariate survival analysis carried out. Responders were defined as patients with partial or complete response and non-responders were defined as patients with stable or progressive disease.

Statistical analysis

Statistical significance was assessed in Prism 7 (GraphPad Software) using either an unpaired, two-tailed Student's t-test, log-rank test, one-way ANOVA or two-way ANOVA, as indicated. $P \leq 0.05$ were considered statistically significant (* $P < 0.05$, ** $P < 0.01$, *** $P < 0.001$, **** $P < 0.0001$).

Data availability

Human expression data from human cancer cell lines and patient samples are publicly available in CCLE and TCGA, respectively. Expression data from lung cancer patients treated with ICB are available from the authors upon request. All other raw data are available upon request from the corresponding authors.

RESULTS

***In vivo* CRISPR screen identifies tumor-intrinsic determinants of anti-tumor immunity**

It is challenging to carry out large scale genome-wide screens *in vivo*, whilst also maintaining a sufficiently high representation of the pooled library, as there is a limit on the number of cells that can be orthotopically transplanted. Instead, a rationally selected, smaller, customized library was used. First, we generated a library of lentiviral vectors encoding sgRNAs targeting 240 genes that are regulated by KRAS in human LUAD. KRAS-regulated genes were identified by differential gene expression analysis of TCGA LUAD samples and LUAD cell lines from the Cancer Cell Line Encyclopedia (CCLE) which were stratified as having high or low RAS pathway activity using a novel 84 gene RAS transcriptional meta-signature derived from multiple RAS pathway signatures (30). Additional genes were identified using RNA-seq data from KRAS^{G12C}-mutant LUAD cell lines (H358 and H23) treated with a KRAS inhibitor and immortalized type II pneumocytes expressing an ER-KRAS^{G12V} fusion protein which can be readily activated by administration of 4-hydroxytamoxifen (4-OHT) (15). To carry out the screen we utilized the immunogenic KPAR cell line, derived from a genetic KRAS^{G12D} p53^{-/-} (KP) lung cancer mouse model as it stimulates endogenous anti-tumor immune responses and is partially responsive to immunotherapy (17). Next, we engineered KPAR cells to express Cas9 under a doxycycline-inducible promoter (Supplementary Fig. 1A). An inducible system was chosen as it allows temporal control of editing and circumvents any compounding consequences of Cas9 immunogenicity *in vivo*. Importantly, Cas9 expression was abrogated *in vitro* 48 hours after the removal of doxycycline (Supplementary Fig. 1B) and was not re-expressed *in vivo* (Supplementary Fig. 1C).

Library-transduced KPAR iCas9 cells were treated with doxycycline for four days to allow gene-editing to occur followed by a two-day washout period to abrogate the expression of Cas9 before orthotopic transplantation into C57BL/6 (WT) mice or *Rag2*^{-/-}; *Il2rg*^{-/-} mice which lack T cells, B cells and NK cells and therefore do not exert anti-tumor immune responses (Fig. 1A). After three weeks, genomic DNA was isolated from tumor-bearing lungs and subject to deep next-generation sequencing (NGS) to compare

library representation in tumors growing in immune-competent and immune-deficient mice (Supplementary Table 1). In parallel, NGS of genomic DNA from cells passaged *in vitro* was carried out to identify genes that affect cell viability. Analysis of genes targeted by sgRNAs that were depleted *in vitro* identified a number of genes known to affect cell viability in KRAS-mutant tumor cells, including *Myc* (32) and *Fos11* (33), thereby validating the functionality of the sgRNA library (Fig. 1B). Furthermore, a number of sgRNAs were equally depleted in immune-competent and immune-deficient mice compared to *in vitro* passaged cells, including those targeting the EMT regulator *Zeb1* and the anti-apoptotic caspase inhibitor c-FLIP (encoded by *Cflar*) (Fig. 1C). These genes therefore supported tumor growth *in vivo* by mechanisms independent of anti-tumor immunity.

By comparing sgRNAs that were depleted or enriched in immune-competent compared to immune-deficient mice we identified genes that modulate anti-tumor immune responses (Fig. 1D). The most enriched sgRNAs in immune-competent mice were targeting a subunit of the IFN γ receptor (*Ifngr2*) (Fig. 1E). Furthermore, we also saw enrichment of sgRNAs targeting the Ets transcription factor ETV4 (Supplementary Fig. 1D). Importantly, *Etv4*^{-/-} KPAR tumors grew faster than parental tumors in WT mice but not in *Rag2*^{-/-}; *Il2rg*^{-/-} mice (Supplementary Fig. 1E), confirming a role for ETV4 in sensitising tumors to anti-tumor immune responses. Indeed, gene expression analysis of *Etv4*^{-/-} KPAR tumors demonstrated that loss of ETV4 resulted in a drastic downregulation of multiple anti-tumor immunity genes (Supplementary Fig. 1F). Conversely, the most depleted sgRNAs in immune-competent mice targeted the prostaglandin synthase COX-2, encoded by *Ptgs2* (Fig. 1F). In addition, sgRNAs targeting the secreted protein endothelin-1, encoded by *Edn1*, were also depleted in immune-competent mice (Supplementary Fig. 1G). Confirming the role of tumor-derived EDN1 in facilitating immune evasion, *Edn1*^{-/-} KPAR tumors grew slower than parental tumors specifically in immune-competent mice (Supplementary Fig. 1H).

KRAS suppresses anti-tumor immunity by inhibition of tumor-intrinsic IFN γ signaling

Tumor-intrinsic IFN γ signaling has previously been shown to be required for anti-tumor immune responses in carcinogen-induced mouse models of cancer (34) and responses to immunotherapy in melanoma (35). To validate the role of tumor-intrinsic IFN γ signaling in anti-tumor immune responses uncovered in the screen we generated *Ifngr2*^{-/-} KPAR cell lines using CRISPR-Cas9 (Supplementary Fig. 2A). As expected, *Ifngr2*^{-/-} KPAR cells were insensitive to IFN γ *in vitro* (Supplementary Fig. 2B). Whilst *Ifngr2*^{-/-} cells grew similarly to parental cells *in vitro* (Supplementary Fig. 2C), they grew faster than parental cells when transplanted into immune-competent mice (Fig. 1G). In contrast *Ifngr2*^{-/-} and parental tumors grew at similar rates in immune-deficient *Rag2*^{-/-}; *Il2rg*^{-/-} mice. These data were validated using a second clone (Supplementary Fig. 2D) indicating that intact tumor-intrinsic IFN γ signaling is required for effective anti-tumor immunity.

IFN γ has been shown to have direct anti-proliferative effects in human cancer cell lines (35). However, the growth of KPAR cells *in vitro* was unaffected by treatment with IFN α , IFN β or IFN γ (Supplementary Fig. 2E). Tumor-intrinsic IFN γ signaling also regulates the expression of antigen presentation machinery and T cell chemoattractants. *Ifngr2*^{-/-} KPAR cells failed to upregulate IFN signaling molecules, IFN-response genes and antigen presentation machinery genes upon treatment with IFN γ (Supplementary Fig. 2F). Furthermore, *Ifngr2*^{-/-} KPAR cells were unable to upregulate PD-L1 or MHC-I surface expression in response to IFN γ , but remained sensitive to type I (IFN α and IFN β) interferons (Supplementary Fig. 2G). Consistent with this, CD45⁻ cells, which includes tumor and stromal cells, had reduced surface expression of MHC-I and PD-L1 in *Ifngr2*^{-/-} KPAR tumors (Supplementary Fig. 2H). In agreement with the hypothesis that tumor-intrinsic IFN γ signaling is required anti-tumor immunity, *Ifngr2*^{-/-} KPAR tumors had less central memory (CD62L⁺CD44⁺) CD8⁺ T cells (T_{cm}) which are important for durable anti-tumor immune responses (Supplementary Fig. 2I). Furthermore, several genes involved in cytotoxic anti-tumor immune responses were downregulated in *Ifngr2*^{-/-} tumors (Supplementary Fig. 2J).

Previous studies have demonstrated that oncogenic KRAS regulates tumor-intrinsic IFN pathway gene expression (15). Indeed, treatment of KPAR cells with the MEK inhibitor trametinib (MEKi), or a previously published three-drug KRAS pathway

inhibitor combination (26) of trametinib, everolimus and linsitinib (TEL), resulted in upregulation of the IFN γ -receptor β subunit (Supplementary Fig. 3A). Moreover, the transcriptional upregulation of IFN-response genes in KPAR cells treated *in vitro* with IFN γ or IFN α was greatly potentiated by MEKi treatment, validating previous results in other lung cancer models (Supplementary Fig. 3B-C). The oncogene Myc acts as a transcriptional suppressor of type I IFN-response genes in pancreatic cancer (36) and we have recently shown that Myc mediates KRAS-driven inhibition of IFN-response genes in lung cancer (15). Myc expression is often driven by KRAS and treatment of KPAR cells with MEKi led to rapid downregulation of Myc (Supplementary Fig. 3D). Consistent with its role in suppressing IFN-responses we saw increased expression of IFN-genes in Myc-depleted cells treated with IFN γ (Supplementary Fig. 3E). Furthermore, Myc-depletion led to increased expression of IFN signaling molecules which were not further upregulated upon treatment with MEKi (Supplementary Fig. 3F), suggesting that oncogenic KRAS suppresses tumor-intrinsic IFN responses by driving expression of Myc. In summary, these data suggest that KRAS-mediated inhibition of tumor-intrinsic IFN γ responses, which is required for effective anti-tumor immunity, may contribute to immune evasion in KRAS-mutant lung cancer.

Tumor-intrinsic COX-2 suppresses innate and adaptive anti-tumor immunity

Ptgs2 loss was the strongest sensitiser to anti-tumor immunity in the screen and encodes the enzyme COX-2 which is overexpressed in many cancer types. COX-2 is responsible for the synthesis of the prostanoid PGE $_2$, which has been shown to suppress anti-tumor immunity in preclinical models of colorectal cancer and melanoma (37). To validate the results obtained in the screen, we began by generating *Ptgs2*^{-/-} KPAR cell lines using CRISPR-Cas9. Western blotting confirmed the loss of COX-2 expression and PGE $_2$ production in *Ptgs2*^{-/-} cells (Supplementary Fig. 4A). We did not observe any difference in the growth of *Ptgs2*^{-/-} cells and parental cells *in vitro* (Supplementary Fig. 4B). However, they grew considerably slower when orthotopically transplanted into immune-competent mice, which as a result had significantly increased survival, with 60% of mice experiencing complete tumor rejection (Fig. 1H). Importantly, COX-2-deficient tumors grew similarly to parental tumors when transplanted into

immune-deficient *Rag2*^{-/-};*Il2rg*^{-/-} mice. This was further validated using a second clone (Supplementary Fig. 4C). Therefore, *Ptgs2*^{-/-} cell lines showed no cell-autonomous defects in tumor progression but were instead sensitized to anti-tumor immune responses, with immunological rejection occurring in a substantial proportion of mice.

As *Rag2*^{-/-};*Il2rg*^{-/-} mice lack NK cells, T cells and B cells, we wanted to decipher the contribution of innate and adaptive immunity to the reduced growth of COX-2-deficient tumors in immune-competent mice. COX-2-deficient tumors grew faster in mice treated with antibodies depleting either NK cells or CD8⁺ T cells and grew fastest in mice lacking both subsets (Fig. 2A, Supplementary Fig. 4D). Interestingly, tumors grew faster in mice lacking NK cells compared to mice lacking CD8⁺ T cells, suggesting the innate immune response was critical for the impaired growth of COX-2-deficient tumors, as previously reported (31). However, no mice survived long-term in the absence of CD8⁺ T cells, demonstrating that the combined action of innate and adaptive immunity was required for tumor rejection. NK cells play a critical role in the control of orthotopic lung tumors during tumor cell seeding in the lung. To ensure the control of COX-2-deficient tumors was not exacerbated by the route of injection we also compared the growth of subcutaneous parental and *Ptgs2*^{-/-} tumors. Similar to the orthotopic setting, COX-2-deficient subcutaneous tumors grew significantly slower in immune-competent mice (Supplementary Fig. 4E). Consistent with the role of both innate and adaptive immunity in the rejection of COX-2-deficient tumors, we observed by flow cytometry increased frequencies of CD8⁺ T cells and NK cells as well as CD4⁺ T cells and Tregs in orthotopic *Ptgs2*^{-/-} lung tumors (Fig. 2B, Supplementary Fig. 5A-B). Increased infiltration of COX-2-deficient tumors by NK cells was confirmed by immunohistochemistry (Fig. 2C). We have previously shown that re-activation of the endogenous ecotropic murine leukaemia retrovirus (eMLV) in KPAR tumors drives anti-tumor T cell responses (17). Indeed, we observed by IFN γ ELISPOT that *Ptgs2*^{-/-} tumors induced an expansion of eMLV-specific CD8⁺ T cells validating the contribution of T cells to the rejection of *Ptgs2*^{-/-} tumors (Supplementary Fig. 6A).

Further flow cytometry analysis revealed drastic changes in the phenotype of both myeloid and adaptive immune subtypes within COX-2-deficient tumors. T cells infiltrating *Ptgs2*^{-/-} tumors were more activated, with higher frequencies of effector

memory (CD44⁺CD62L⁻) CD8⁺ and CD4⁺ T cells (T_{em}) (Fig. 2D), mirrored by fewer naïve (CD44⁻CD62L⁺) T cells, an increased frequency of T cells expressing checkpoint receptors (Supplementary Fig. 6B) and upregulation of the activation markers CD44 and CD69 (Fig. 2E, Supplementary Fig. 6C). T cell-mediated immune responses require priming by CD103⁺ dendritic cells (DCs) both in lymph nodes and within tumors. Tumor-derived prostaglandins have previously been reported to prevent the accumulation of CD103⁺ DCs into the TME (37), however we did not see increased CD103⁺ DCs in *Ptgs2*^{-/-} tumors (Supplementary Fig. 6D). Despite this, we observed increased expression of the co-stimulatory molecule CD86 and MHC-II on CD103⁺ DCs (Supplementary Fig. 6E). Similarly, loss of COX-2 did not alter the frequency of tumor-associated macrophages (TAMs) (Supplementary Fig. 6F) but induced pro-inflammatory polarisation of both CD11b⁺ and CD11c⁺ TAMs with increased expression of both CD86 and MHC-II (Fig. 2F, Supplementary Fig. 6G) as well as decreased expression of the M2 markers arginase and CD206 (Fig. 2G-H, Supplementary Fig. 6H). Indeed, when assessing the frequency of M1 (MHC-II⁺CD206⁻) and M2 (MHC-II⁻CD206⁺) CD11b⁺ TAMs we observed a dramatic increase of the M1/M2 ratio in COX-2-deficient tumors (Fig. 2I). *Ptgs2*^{-/-} tumors also had fewer immunosuppressive Ly6C⁺ monocytes (Supplementary Fig. 6I). In addition, several myeloid subtypes, including CD11b⁺ TAMs, CD103⁺ DCs, CD11b⁺ DCs and neutrophils, exhibited increased PD-L1 expression (Supplementary Fig. 6J), characteristic of a T-cell inflamed TME. Gene expression analysis resulted in distinct clustering of parental KPAR and *Ptgs2*^{-/-} tumors with COX-2 loss leading to increased expression of genes encoding Th1 cytokines (*Ifng*, *Tnfa*, *Cxcl9*), cytotoxicity genes (*Gzmb*, *Prf1*), IFN-response genes (*Irf9*, *B2m*, *Stat1*) and decreased expression of the immunosuppressive cytokine IL-6 (Fig. 2J). Together these data suggests that loss of tumor-intrinsic expression of COX-2 results in a remodelling of the tumor microenvironment with increased recruitment of effector cells and polarisation of both innate and adaptive immune subsets towards a pro-inflammatory phenotype resulting in enhanced anti-tumor immunity and greater tumor control.

COX-2/PGE₂ signaling drives resistance to ICB in mouse and human LUAD

Given that tumor-intrinsic COX-2 acts as a major driver of immune evasion in KPAR tumors we wanted to assess whether it also contributed to resistance to ICB. Mice were orthotopically transplanted with parental KPAR or *Ptgs2*^{-/-} cells and treated with anti-PD-1. Whilst parental KPAR tumors were partially responsive to anti-PD-1, COX-2 deficient tumors were significantly more sensitive to PD-1 blockade with all ICB-treated mice bearing *Ptgs2*^{-/-} lung tumors surviving long-term (Fig. 3A). Immunohistochemistry revealed that similar to ICB-treated KPAR tumors, *Ptgs2*^{-/-} lung tumors were more infiltrated by CD8⁺ T cells (Fig. 3B), confirming what we observed by flow cytometry (Fig. 2B), however the biggest increase was seen in ICB-treated *Ptgs2*^{-/-} tumors. Furthermore, flow cytometry analysis demonstrated that PD-1 blockade only led to increased activation of CD8⁺ T cells in *Ptgs2*^{-/-} lung tumors (Fig. 3C). In addition, ICB-treated *Ptgs2*^{-/-} lung tumors showed the greatest expansion of effector memory CD8⁺ T cells (Supplementary Fig. 7A) and upregulation of checkpoint molecules (Fig. 3D). Interestingly, anti-PD-1 treatment also led to increased NK cell infiltration in *Ptgs2*^{-/-} lung tumors, which did not occur in KPAR tumors (Supplementary Fig. 7B). Furthermore, gene expression analysis revealed that anti-PD-1 induced robust expression of anti-tumor immunity genes only in COX-2-deficient lung tumors (Fig. 3E, Supplementary Fig. 7C). Together these data suggest that tumor-intrinsic COX-2 promotes resistance to ICB by preventing the stimulation of anti-tumor immunity in response to PD-1 blockade.

To determine whether COX-2/PGE₂ signaling also affected the clinical response of lung cancer patients to immunotherapy we examined the expression of a previously published COX-2-associated inflammatory gene expression signature (COX-IS) (31) in a cohort of LUAD patients treated with anti-PD-L1/PD-1 for which baseline expression data was available (38). Importantly, expression of the COX-IS was significantly higher in LUAD patients who did not respond to ICB (Fig. 3F). Furthermore, higher COX-IS expression was associated with significantly worse progression-free survival following ICB (Fig. 3G) and was also predictive of outcome independent of age, gender, smoking status and previous lines of therapy (Fig. 3H). These results support the notion, as suggested by the mouse model, that the COX-2/PGE₂ axis drives immunosuppression and hinders response to ICB in human LUAD.

Inhibition of the COX-2/PGE₂ axis delays tumor growth and synergises with ICB

Whilst genetic deletion of tumor-intrinsic COX-2 resulted in a drastic repolarisation of the tumor microenvironment, increased tumor control and sensitisation to ICB, we next sought to assess whether pharmacological blockade of COX-2 could have similar effects. We treated KPAR lung tumor-bearing mice with the COX-2 specific inhibitor celecoxib, which was administered by daily oral gavage. As seen in *Ptgs2*^{-/-} lung tumors, treatment of KPAR tumors with celecoxib resulted in polarisation of TAMs with upregulation of CD86 and MHC-II (Fig. 4A, Supplementary Fig. 8A), decreased expression of arginase (Fig. 4B, Supplementary Fig. 8B) and an increase in the M1/M2 ratio (Fig. 4C), as well as reduced infiltration of Ly6C⁺ monocytes (Supplementary Fig. 8C). Changes in the myeloid compartment were accompanied by increased activation of CD8⁺ T cells (Fig. 4D).

Importantly, celecoxib significantly extended the survival of KPAR-tumor bearing mice to a similar extent seen with PD-1 blockade (Fig. 4E). However, the combination of both celecoxib and anti-PD-1 showed superior efficacy compared to either single-agent alone. Indeed, both celecoxib and anti-PD-1 increased infiltration of tumors with CD8⁺ T cells which was further increased in the combination treatment arm (Fig. 4F). Furthermore, only the combination treatment led to a significant expansion of effector memory CD8⁺ T cells (Fig. 4G) and upregulation of checkpoint molecules on both CD8⁺ and CD4⁺ T cells (Supplementary Fig. 8D). Combination treatment also induced the highest levels of PD-L1 on several myeloid cell types (Supplementary Fig. 8E). This could be due to elevated levels of IFN γ (Fig. 4H) which was significantly upregulated in the combination treatment arm along with other anti-tumor immunity genes.

In the clinic, celecoxib has been associated with increased cardiovascular risk (39), which prompted us to explore other therapeutic options to target this immunosuppressive axis. Immune cells express four receptors for PGE₂, EP1-4. However, numerous studies have demonstrated EP2 and EP4 receptors are the primary mediators of the COX-2/PGE₂ immunosuppressive axis (40,41). We therefore treated tumor-bearing mice with a novel dual EP2-EP4 antagonist TPST-1495 (42). As seen with celecoxib, dual EP2-EP4 inhibition led to a significant increase in the M1/M2

macrophage ratio (Fig. 5A) with reduced expression of arginase (Fig. 5B), as well as increased activation of CD8⁺ T cells (Fig. 5C). Indeed, TPST-1495 increased the survival of tumor-bearing mice similarly to PD-1 blockade (Fig. 5D). The combination of TPST-1495 and anti-PD-1 also significantly extended the survival of mice compared to either monotherapy, with greater synergy as compared to the combination of celecoxib and anti-PD-1. Furthermore, gene expression analysis revealed distinct clustering of tumors treated with the combination with potent induction of a pro-inflammatory transcriptional program (Fig. 5E-F). Consistent with this, the combination treatment led to the biggest increase in PD-L1 expression on tumor-infiltrating myeloid cells (Supplementary Fig. 8F). In conclusion, these results suggest that pharmacological inhibition of the COX-2/PGE₂ axis reverses immunosuppression in the TME, promoting adaptive immunity which enhances the therapeutic efficacy of ICB.

COX-2 expression is driven by oncogenic KRAS and contributes to tumor relapse after KRAS^{G12C} inhibition

Given the known role of oncogenic KRAS in mediating immune evasion we next wanted to understand whether tumor-intrinsic COX-2 expression was regulated by KRAS signaling. To test this, we inhibited KRAS signaling in several mouse and human KRAS-mutant cancer cell lines. Firstly, treatment of KPAR cells *in vitro* with the MEK inhibitor trametinib led to a drastic reduction in COX-2 protein expression and loss of PGE₂ secretion (Fig. 6A). We validated this in the 3LL Δ NRAS mouse lung cancer cell line (26), which contains a KRAS^{G12C} mutation and has been rendered sensitive to KRAS^{G12C} inhibitors by deletion of oncogenic NRAS, as well as the CT26^{G12C} colorectal cancer cell line (27) and the KPAR^{G12C} cell line (17) which have been engineered to express KRAS^{G12C} (Supplementary Fig. 9A). Treatment with the KRAS^{G12C} inhibitor MRTX849 led to reduced COX-2 expression (Fig. 6B) and loss of PGE₂ secretion in all three cell lines (Fig. 6C). Inhibition of oncogenic KRAS using the KRAS^{G12D} mutant-specific inhibitor MRTX1133 also resulted in a reduction in COX-2 expression in the KPAR^{G12D} cell line (Supplementary Fig. 9B-C). Importantly, celecoxib significantly delayed the growth of 3LL Δ NRAS tumors (Supplementary Fig. 9D) and has recently been shown to reduce the growth of CT26 tumors (41). To extend these findings *in vivo*

we carried out gene expression analysis of KP GEMM or KPAR tumors from mice treated with MEKi or TEL, respectively, and observed a decrease in the expression of COX-2 mRNA (Supplementary Fig. 9E-F). MEKi inhibits MAPK signaling in stromal and immune cells as well as tumor cells so we also assessed COX-2 expression levels in 3LL Δ NRAS and KPAR^{G12C} tumors from mice treated with MRTX849, as KRAS^{G12C} inhibitors only target tumor cells. KRAS^{G12C} inhibition downregulated COX-2 mRNA expression in both 3LL Δ NRAS and KPAR^{G12C} tumors (Fig. 6D). This was accompanied by a decrease in COX-2 protein expression (Supplementary Fig. 9G) in KPAR^{G12C} tumors from mice treated with MRTX849. Furthermore, in both tumor models KRAS^{G12C} inhibition reduced the expression of the COX-2-associated inflammatory signature COX-IS (Fig. 6E).

Consistent with our results in mouse cancer cell lines, we also observed significant downregulation of COX-2 expression in a panel of KRAS^{G12C} human LUAD cell lines treated *in vitro* with MRTX849 (Fig. 6F). Importantly, such an effect was not observed in KRAS^{G12S} A549 cells which are insensitive to KRAS^{G12C} inhibition. The KRAS^{G12C} human cell lines differed in their sensitivity to KRAS^{G12C} inhibition (Supplementary Fig. 9H) suggesting that the downregulation of COX-2 was not due to drug-induced cytotoxicity. We extended our analysis using expression data from human lung cancer cell lines from the CCLE database which were classified as either having high or low oncogenic RAS pathway activity based on the 84 gene RAS transcriptional signature (30). We observed significantly increased expression of *PTGS2* in high-RAS pathway activity cell lines (Fig. 6G). Similarly, *PTGS2* expression was increased in KRAS-mutant cell lines (Supplementary Fig. 9I). We also analysed LUAD expression data from TCGA which were stratified by hierarchical clustering into five different groups, RAG-0 to RAG-4, based on expression of the RAS activity transcriptional signature, with RAG-0 being the lowest and RAG-4 being the highest. COX-IS was significantly increased in all RAS active groups with highest levels occurring in RAG-1 and RAG-3 which are associated with co-occurring *STK11/LKB1* or *TP53* mutations, respectively (Fig. 6H). Similarly, *PTGS2* mRNA levels were elevated in RAS active tumors as well as KRAS-mutant tumors (Supplementary Fig. 9J). Interestingly, COX-IS was not elevated in KRAS-mutant tumors (Supplementary Fig. 9K) demonstrating the advantage of

utilising a RAS transcriptional signature, rather than simply KRAS mutation status, to capture RAS signaling activity in human lung cancer.

The advent of KRAS^{G12C} inhibitors has transformed the treatment landscape for KRAS^{G12C}-mutant lung cancer patients. However, responses are often short-lived and combination therapies will be required to overcome the development of adaptive resistance. Whilst oncogenic KRAS pathway reactivation will re-engage proliferative signaling, we postulated that restoration of KRAS-mediated immunosuppression may also contribute to tumor relapse. Interestingly, COX-2 expression was restored in KPAR^{G12C} cells *in vitro* after long-term MRTX849 treatment (Fig. 6I) and *in vivo* in KPAR^{G12C} tumors that relapsed after MRTX849 treatment (Fig. 6J). Upregulated expression of multiple KRAS target genes (*Dusp4*, *Dusp5*, *Dusp6*) in MRTX-relapsed tumors confirmed the reactivation of KRAS pathway signaling *in vivo* (Supplementary Fig. 9L). Importantly, the combination of MRTX849 and celecoxib delayed tumor relapse and significantly improved the survival of KPAR^{G12C} tumor-bearing mice compared to MRTX849 alone (Fig. 6K).

In summary, these data suggest that oncogenic KRAS is a major driver of COX-2/PGE₂ signaling in mouse and human lung cancer and may therefore contribute to ICB resistance in KRAS-mutant LUAD and tumor relapse in patients treated with KRAS^{G12C} inhibitors which can be overcome by COX-2/PGE₂ pathway inhibitors.

DISCUSSION

A subset of KRAS-mutant lung cancer patients has greatly benefited from the advent of immune checkpoint blockade therapy. However, the majority of patients still do not respond. Combination strategies are urgently required to broaden the efficacy of immunotherapy. Accumulating evidence suggests that tumor-intrinsic oncogenic signaling can dampen anti-tumor immune responses (30) which could be therapeutically exploited to overcome immunotherapy resistance in specific tumor subtypes, but little progress has been made to date in attempts to combine immunotherapies with therapies targeting oncogenic signaling pathways. Here, we carried out *in vivo* CRISPR screening using a novel immunogenic model of KRAS-mutant lung adenocarcinoma (17) to uncover multiple mechanisms by which oncogenic KRAS drives immune evasion, with a view to inform the development of optimal combination strategies for targeting KRAS mutant cancers that impact both oncogenic signaling and immune evasion.

We demonstrated that tumor-intrinsic IFN γ signaling is critical for anti-tumor immunity. Indeed, numerous CRISPR screens have demonstrated that defects in IFN γ signaling result in resistance to immunotherapy (21,43) and mutations in *JAK1* and *JAK2* have been associated with acquired resistance to ICB (44). Given the importance of tumor-intrinsic IFN γ signaling in sensitising KPAR tumors to anti-tumor immune responses, the ability of oncogenic KRAS to suppress IFN pathway signaling may represent a major mechanism of immune evasion in KRAS-mutant LUAD. These results are consistent with our previous findings that KRAS^{G12C} inhibitors can restore tumor-intrinsic IFN signaling in multiple preclinical models of lung cancer (15). Paradoxically, tumor-intrinsic IFN γ signaling has also been shown to impede anti-tumor immunity (45), including in a CRISPR screen using an orthotopic KRAS^{G12D} p53^{-/-} lung cancer model similar to the one used in this study (25). Whilst such opposing effects in similar models are surprising, chronic tumor-intrinsic IFN γ signaling can drive resistance to ICB due to upregulation of immune checkpoint ligands (46). Understanding the contexts in which tumor-intrinsic IFN γ signaling promotes or impedes anti-tumor immunity will be important when assessing combination strategies targeting this pathway.

We also identified KRAS-driven expression of COX-2 and secretion of PGE₂ as a major mechanism of immune evasion which suppresses both innate and adaptive anti-tumor immune responses. This is consistent with the role of tumor-intrinsic COX-2 in driving immune evasion in melanoma and colorectal cancer (37). The ability of our CRISPR screen to elucidate the function of a secreted molecule can be explained by a recent barcoded CRISPR screen which demonstrated that orthotopic KP tumors grow as clonal lesions (25), suggesting that local secretion of a particular molecule by neighbouring tumor cells that do not contain the same gene deletion is unlikely to be a major problem.

COX-2 derived PGE₂ is a pleiotropic molecule that has been shown to act on many cell types including CD8⁺ T cells, dendritic cells and NK cells (47), although single-cell sequencing studies have revealed EP2 and EP4 receptors to be highly expressed specifically on tumor-infiltrating myeloid cells (48). Indeed, we observed extensive changes in the TME of COX-2-deficient tumors including pro-inflammatory polarisation of myeloid cells and concomitant infiltration of highly activated CD8⁺ T cells and NK cells. Interestingly, NK cell depletion was best able to restore the growth of COX-2-deficient tumors. Whilst NK cells play a major role in the control of orthotopic lung cancer models, we also observed reduced growth of COX-2-deficient subcutaneous tumors as early as 7 days, before the onset of an adaptive immune response. This is consistent with the observation that PGE₂ directly suppresses the survival of NK cells (49) which are required to drive remodelling of the tumor microenvironment, including pro-inflammatory polarisation of macrophages and activation of CD8⁺ T cells, and promote immune-control in COX-2-deficient melanoma tumors (31). The dramatic reduction of survival upon NK cell depletion also suggests a role for direct tumor cell killing which we have previously shown to be mediated by antibody-dependent cellular cytotoxicity in the KPAR model (50). Furthermore, the effects we observed of tumor-derived PGE₂ on myeloid cells are consistent with a recent study that demonstrated the immunosuppressive role of PGE₂-producing lung fibroblasts which promote breast cancer metastasis (40). The role of COX-2 expressing lung fibroblasts within primary lung tumors remains unclear, however our results suggest that the majority of PGE₂ secretion within the TME is derived from tumor cells,

as tumor-specific genetic deletion of COX-2 was sufficient to drive immune-mediated tumor eradication. Unlike studies in melanoma (37), we did not observe increased CD103⁺ DC recruitment in COX-2-deficient tumors, reflecting the context-specific effects of prostaglandin signaling in different tumor types. CD103⁺ DCs have a unique ability to prime CD8⁺ T cells and the increased expression of co-stimulatory molecule expression on CD103⁺ DCs in *Ptgs2*^{-/-} tumors may explain the enhanced T cell activation observed. A recent study utilising the syngeneic 3LL/LLC Lewis lung cancer model described a role for Tregs in mediating the immunosuppressive effects of the COX-2/PGE₂ signaling axis in subcutaneous tumors (48) which we did not observe in our experimental model system. This may be explained by differences in anti-tumor immune responses observed in orthotopic versus subcutaneous tumors. Indeed, multiple transplantable lung cancer models have been shown to have abundant infiltration of Tregs in subcutaneous tumors compared to orthotopic lung tumors (17,51). COX-2 deficient tumors exhibited increased abundance of Tregs which is consistent with murine experiments demonstrating that CD8⁺ T cells can drive Treg infiltration into the TME (52).

Our data demonstrates the therapeutic benefits of genetic ablation or pharmacological inhibition of COX-2 in a preclinical model of KRAS-mutant lung cancer, especially in combination with immunotherapy. Furthermore, the ability of the COX-IS to independently predict outcome after ICB suggests a role for COX-2/PGE₂ signaling in hindering responses to ICB in LUAD patients, supporting previous findings in other cancer types (31). Given that the expression of the COX-IS was strongly driven by oncogenic KRAS signaling in both mouse and human lung cancer, our studies suggest that inhibiting the COX-2/PGE₂ axis is a promising therapeutic strategy in KRAS-mutant NSCLC and may broaden the efficacy of immune checkpoint blockade for these patients. Interestingly, our analysis of COX-IS expression in the LUAD TCGA cohort demonstrated increased activity of the COX-2/PGE₂ axis in RAG-1 patients, which are associated with STK11/LKB1 co-occurring mutations. These patients respond poorly to ICB (53) and therefore may particularly benefit from this combination therapy.

Indeed, a number of clinical trials are currently testing the combination of celecoxib with immune checkpoint blockade (NCT03026140, NCT03864575). However, these trials do not specifically enrol KRAS-mutant LUAD patients which our data suggests would most benefit from such a combination. The potential benefit of this combination is supported by a recent retrospective analysis showing improved survival of lung cancer patients that were concurrently treated with COX inhibitors whilst receiving immunotherapy (54). Furthermore, we show using a novel drug that dual inhibition of the PGE₂ receptors EP2 and EP4 has similar therapeutic benefits to COX-2 inhibition and shows superior synergy when combined with ICB. This supports other work in preclinical models that have demonstrated the benefits of combining EP2 and EP4 antagonists with ICB (40,41,55). EP2 and EP4 inhibition therefore has the potential to enhance the efficacy of immunotherapy in the clinic, whilst possibly avoiding the toxicities associated with celecoxib treatment, including those associated with inhibition of other targets of PGE₂, including the EP1 and EP3 receptors.

The ability of KRAS^{G12C} inhibition to suppress the COX-2/PGE₂ signaling axis *in vivo* may in part explain the synergy observed in combination with ICB in preclinical models (15,17,18,27). However, given the apparent poor tolerability of the combination of KRAS^{G12C} inhibition by sotorasib and PD(L)-1-targeted ICB observed in the clinic (19), it may be more feasible to target KRAS-driven immune evasion mechanisms such as COX-2. The benefits of KRAS^{G12C} inhibition in the clinic are also seriously confounded by the rapid emergence of acquired resistance which can be driven by many different oncogenic mutations within the RAS signaling pathway (11). Clinical trials such as CODEBREAK 101 are attempting to overcome this by combining KRAS^{G12C} inhibitors with other targeted therapies such as RTK inhibitors; however, given the genetic complexity underlying resistance, the feasibility of this approach remains unclear. Instead, targeting KRAS-driven immune suppression may prove more successful. Our work shows that long-term KRAS^{G12C} inhibition results in restoration of the COX-2/PGE₂ axis which may contribute to tumor relapse. Furthermore, our data suggest that combination of KRAS^{G12C} inhibitory drugs and COX-2 or EP2-4 prostaglandin receptor inhibition may be successful in the treatment of immune hot lung cancer and it might be

speculated that it could possibly avoid the toxicities reported for sotorasib and PD(L)-1 blockade.

ACKNOWLEDGEMENTS

We thank the science technology platforms at the Francis Crick Institute including Biological Resources, Advanced Sequencing, Scientific Computing, Bioinformatics and Biostatistics, Flow Cytometry, Experimental Histopathology, and Cell Services.

Funding: This work was supported by the Francis Crick Institute which receives its core funding from Cancer Research UK (FC001070), the UK Medical Research Council (FC001070), and the Wellcome Trust (FC001070). This work also received funding from the European Research Council Advanced Grant RASImmune, and from a Wellcome Trust Senior Investigator Award 103799/Z/14/Z. A.dC. received fellowship support from “La Caixa” Foundation (LCF/BQ/EU21/11890069).

Author contributions: J.B, M.M-A and J.D. designed the study, interpreted the results and wrote the manuscript. J.B., A.dC., S.R., M.T., P.A. and E.M. performed the biochemical experiments, C.M. assisted with *in vivo* studies, N.B., H.C., S.dC.T., P.E. and R.G. performed bioinformatics analyses, S-H.L. and K.L. provided patient data. All authors contributed to manuscript revision and review.

REFERENCES

1. Siegel RL, Miller KD, Fuchs HE, Jemal A. Cancer statistics, 2022. *CA Cancer J Clin.* 2022;72:7–33.
2. Wei SC, Duffy CR, Allison JP. Fundamental mechanisms of immune checkpoint blockade therapy. *Cancer Discov.* 2018;8:1069–86.
3. Borghaei H, Paz-Ares L, Horn L, Spigel DR, Steins M, Ready NE, et al. Nivolumab versus docetaxel in advanced nonsquamous non-small-cell lung cancer. *New England Journal of Medicine.* 2015;373:1627–39.
4. Reck M, Rodriguez-Abreu D, Robinson AG, Hui R, Csösz T, Fülöp A, et al. Pembrolizumab versus Chemotherapy for PD-L1-Positive Non-Small-Cell Lung Cancer. *New England Journal of Medicine.* 2016;375:1823–33.
5. Gandhi L, Rodríguez-Abreu D, Gadgeel S, Esteban E, Felip E, De Angelis F, et al. Pembrolizumab plus chemotherapy in metastatic non-small-cell lung cancer. *New England Journal of Medicine.* 2018;378:2078–92.
6. Collisson EA, Campbell JD, Brooks AN, Berger AH, Lee W, Chmielecki J, et al. Comprehensive molecular profiling of lung adenocarcinoma. *Nature.* 2014;511:543–50.
7. Cox AD, Fesik SW, Kimmelman AC, Luo J, Der CJ. Drugging the undruggable RAS: Mission Possible? *Nat Rev Drug Discov.* 2014;13:828–51.
8. Ostrem JML, Shokat KM. Direct small-molecule inhibitors of KRAS: from structural insights to mechanism-based design. *Nat Rev Drug Discov.* 2016;15:771–85.
9. Prior IA, Hood FE, Hartley JL. The frequency of ras mutations in cancer. *Cancer Res.* 2020;80:2969–74.
10. Skoulidis F, Li BT, Dy GK, Price TJ, Falchook GS, Wolf J, et al. Sotorasib for lung cancers with KRAS p.G12C mutation. *New England Journal of Medicine.* 2021;384:2371–81.
11. Awad MM, Liu S, Rybkin II, Arbour KC, Dilly J, Zhu VW, et al. Acquired resistance to KRAS G12C inhibition in cancer. *New England Journal of Medicine.* 2021;384:2382–93.
12. Wellenstein MD, Visser KE de. Cancer-cell-intrinsic mechanisms shaping the tumor immune landscape. *Immunity.* 2018;48:399–416.
13. Skoulidis F, Byers LA, Diao L, Papadimitrakopoulou VA, Tong P, Izzo J, et al. Co-occurring genomic alterations define major subsets of KRAS-mutant lung adenocarcinoma with distinct biology, immune profiles, and therapeutic vulnerabilities. *Cancer Discov.* 2015;5:861–78.
14. Pylayeva-Gupta Y, Lee KE, Hajdu CH, Miller G, Bar-Sagi D. Oncogenic Kras-induced GM-CSF production promotes the development of pancreatic neoplasia. *Cancer Cell.* 2012;21:836–47.
15. Mugarza E, Maldegem F van, Boumelha J, Moore C, Rana S, Sopena ML, et al. Therapeutic KRASG12C inhibition drives effective interferon-mediated anti-tumor immunity in immunogenic lung cancers. *Sci Adv.* 2021;8:eabm8780.

16. Coelho MA, de Carné Trécesson S, Rana S, Zecchin D, Moore C, Molina-Arcas M, et al. Oncogenic RAS signaling promotes tumor immunoresistance by stabilizing PD-L1 mRNA. *Immunity*. 2017;47:1083–99.
17. Boumelha J, de Carné Trécesson S, Law EK, Romero-Clavijo P, Coelho M, Ng K, et al. An immunogenic model of KRAS-mutant lung cancer enables evaluation of targeted therapy and immunotherapy combinations. *Cancer Res*. 2022;82:3435–48.
18. Canon J, Rex K, Saiki AY, Mohr C, Cooke K, Bagal D, et al. The clinical KRAS (G12C) inhibitor AMG 510 drives anti-tumor immunity. *Nature*. 2019;575:217–23.
19. Li BT, Falchook GS, Durm GA, Burns TF, Skoulidis F, Ramalingam SS, et al. CodeBreak 100/101: First Report of Safety/Efficacy of Sotorasib in Combination with Pembrolizumab or Atezolizumab in Advanced KRAS p.G12C NSCLC. *Journal of Thoracic Oncology*. 2022;17:S10–1.
20. Begum P, Goldin RD, Possamai LA, Popat S. Severe Immune Checkpoint Inhibitor Hepatitis in KRAS G12C-Mutant NSCLC Potentially Triggered by Sotorasib: Case Report. *JTO Clin Res Rep*. 2021;2:100213.
21. Manguso RT, Pope HW, Zimmer MD, Brown FD, Yates KB, Miller BC, et al. In vivo CRISPR screening identifies Ptpn2 as a cancer immunotherapy target. *Nature*. 2017;547:413–8.
22. Pan D, Kobayashi A, Jiang P, Andrade LF De, Tay RE, Luoma A, et al. A major chromatin regulator determines resistance of tumor cells to T cell – mediated killing. *Science*. 2018;359:770–5.
23. Li F, Huang Q, Luster TA, Hu H, Zhang H, Ng WL, et al. In vivo epigenetic CRISPR screen identifies Asf1a as an immunotherapeutic target in Kras-mutant lung adenocarcinoma. *Cancer Discov*. 2020;10:270–87.
24. Griffin GK, Wu J, Iracheta-vellve A, Patti JC, Hsu J, Davis T, et al. Epigenetic silencing by SETDB1 suppresses tumor intrinsic immunogenicity. *Nature*. 2021;595:309–14.
25. Dhainaut M, Rose SA, Akturk G, Wroblewska A, Nielsen SR, Park ES, et al. Spatial CRISPR genomics identifies regulators of the tumor microenvironment. *Cell*. 2022;185:1223-1239.e20.
26. Molina-Arcas M, Moore C, Rana S, van Maldegem F, Mugarza E, Romero-Clavijo P, et al. Development of combination therapies to maximize the impact of KRAS-G12C inhibitors in lung cancer. *Sci Transl Med*. 2019;11:eaaw7999.
27. Briere DM, Li S, Calinisan A, Sudhakar N, Aranda R, Hargis L, et al. The KRAS^{G12C} Inhibitor MRTX849 Reconditions the Tumor Immune Microenvironment and Sensitizes Tumors to Checkpoint Inhibitor Therapy. *Mol Cancer Ther*. 2021;20:975–85.
28. Zaw Thin M, Moore C, Snoeks T, Kalber T, Downward J, Behrens A. Micro-CT acquisition and image processing to track and characterize pulmonary nodules in mice. *Nat Protoc*. 2022;18:990-1015
29. Joung J, Konermann S, Gootenberg JS, Abudayyeh OO, Platt RJ, Brigham MD, et al. Genome-scale CRISPR-Cas9 knockout and transcriptional activation screening. *Nat Protoc*. 2017;12:828–63.

30. East P, Kelly GP, Biswas D, Marani M, Hancock DC, Creasy T, et al. RAS oncogenic activity predicts response to chemotherapy and outcome in lung adenocarcinoma. *Nat Commun.* 2022;13:5632.
31. Bonavita E, Bromley CP, Jonsson G, Pelly VS, Sahoo S, Walwyn-Brown K, et al. Antagonistic inflammatory phenotypes dictate tumor fate and response to immune checkpoint blockade. *Immunity.* 2020;53:1215–29.
32. Soucek L, Whitfield JR, Sodir NM, Massó-Vallés D, Serrano E, Karnezis AN, et al. Inhibition of Myc family proteins eradicates Kras-driven lung cancer in mice. *Genes Dev.* 2013;27:504–13.
33. Vallejo A, Perurena N, Guruceaga E, Mazur PK, Martinez-Canarias S, Zanduetta C, et al. An integrative approach unveils FOSL1 as an oncogene vulnerability in KRAS-driven lung and pancreatic cancer. *Nat Commun.* 2017;8:14294.
34. Dighe AS, Richards E, Old LJ, Schreiber RD. Enhanced in vivo growth and resistance to rejection of tumor cells expressing dominant negative IFN γ receptors. *Immunity.* 1994;1:447–56.
35. Torrejon DY, Abril-Rodriguez G, Champhekar AS, Tsoi J, Campbell KM, Kalbasi A, et al. Overcoming genetically-based resistance mechanisms to PD-1 blockade. *Cancer Discov.* 2020;10:1140–57.
36. Muthalagu N, Monteverde T, Raffo-Iraolagoitia X, Wiesheu R, Whyte D, Hedley A, et al. Repression of the type I interferon pathway underlies MYC- and KRAS-dependent evasion of NK and B Cells in pancreatic ductal adenocarcinoma. *Cancer Discov.* 2020;10:872–87.
37. Zelenay S, Van Der Veen AG, Böttcher JP, Snelgrove KJ, Rogers N, Acton SE, et al. Cyclooxygenase-Dependent Tumor Growth through Evasion of Immunity. *Cell.* 2015;162:1257–70.
38. Park S, Cha H, Kim HS, Lee B, Kim S, Kim TM, et al. Transcriptional upregulation of CXCL13 is correlated with a favorable response to immune checkpoint inhibitors in lung adenocarcinoma. *Cancer Med.*; 2022;0:1–12.
39. Solomon SD, McMurray JJV, Pfeffer MA, Wittes J, Fowler R, Finn P, et al. Cardiovascular risk associated with celecoxib in a clinical trial for colorectal adenoma prevention. *New England Journal of Medicine.* 2005;352:1071–80.
40. Gong Z, Li Q, Shi J, Wei J, Li P, Chang CH, et al. Lung fibroblasts facilitate pre-metastatic niche formation by remodeling the local immune microenvironment. *Immunity.* 2022;55:1483-1500.e9.
41. Pelly VS, Moeini A, Roelofsen LM, Bonavita E, Bell CR, Hutton C, et al. Anti-inflammatory drugs remodel the tumor immune environment to enhance immune checkpoint blockade efficacy. *Cancer Discov.* 2021;11:2602–19.
42. Davar D, Powderly JD, Varkey Ulahannan S, Lynne Johnson M, Sharma M, Krauss JC, et al. A phase 1 study of TPST-1495 as a single agent and in combination with pembrolizumab in subjects with solid tumors. *Journal of Clinical Oncology.* 2022;40:TPS2696.
43. Kearney CJ, Vervoort SJ, Hogg SJ, Ramsbottom KM, Freeman AJ, Lalaoui N, et al. Tumor immune evasion arises through loss of TNF sensitivity. *Sci Immunol.* 2018;3:eaar3451.

44. Zaretsky JM, Garcia-Diaz A, Shin DS, Escuin-Ordinas H, Hugo W, Hu-Lieskovan S, et al. Mutations associated with acquired resistance to PD-1 blockade in melanoma. *New England Journal of Medicine*. 2016;375:819–29.
45. Dubrot J, Du PP, Lane-Reticker SK, Kessler EA, Muscato AJ, Mehta A, et al. In vivo CRISPR screens reveal the landscape of immune evasion pathways across cancer. *Nat Immunol*. 2022;23:1495–506.
46. Benci JL, Xu B, Qiu Y, Wu TJ, Dada H, Twyman-Saint Victor C, et al. Tumor Interferon Signaling Regulates a Multigenic Resistance Program to Immune Checkpoint Blockade. *Cell*. 2016;167:1540-1554.e12.
47. Liu B, Qu L, Yan S. Cyclooxygenase-2 promotes tumor growth and suppresses tumor immunity. *Cancer Cell Int*. 2015;15:106.
48. Thumkeo D, Punyawatthanakool S, Prasongtanakij S, Matsuura R, Arima K, Nie H, et al. PGE2-EP2/EP4 signaling elicits immunosuppression by driving the mregDC-Treg axis in inflammatory tumor microenvironment. *Cell Rep*. 2022;39:10914
49. Böttcher JP, Bonavita E, Chakravarty P, Blees H, Cabeza-Cabrerizo M, Sammicheli S, et al. NK Cells stimulate recruitment of cDC1 into the tumor microenvironment promoting cancer immune control. *Cell*. 2018;172:1022–37.
50. Ng KW, Boumelha J, Enfield KSS, Almagro J, Cha H, Pich O, et al. Antibodies against endogenous retroviruses promote lung cancer immunotherapy. *Nature* 2023; 616:563-73
51. Li HY, Mcsharry M, Bullock B, Nguyen TT, Kwak J, Poczobutt JM, et al. The tumor microenvironment regulates sensitivity of murine lung tumors to PD-1 / PD-L1 antibody blockade. *Cancer Immunol Res*. 2017;5:767–78.
52. Spranger S, Spaapen RM, Zha Y, Williams J, Meng Y, Ha TT, et al. Up-regulation of PD-L1, IDO, and Tregs in the melanoma tumor microenvironment is driven by CD8⁺ T cells. *Sci Transl Med*. 2013;5:200ra116.
53. Skoulidis F, Goldberg ME, Greenawalt DM, Hellmann MD, Awad MM, Gainor JF, et al. STK11/LKB1 mutations and PD-1 inhibitor resistance in KRAS- mutant lung adenocarcinoma. *Cancer Discov*. 2018;8:822–35.
54. Wang SJ, Khullar K, Kim S, Yegya-Raman N, Malhotra J, Groisberg R, et al. Effect of cyclo-oxygenase inhibitor use during checkpoint blockade immunotherapy in patients with metastatic melanoma and non-small cell lung cancer. *J Immunother Cancer*. 2020;8:e000889.
55. Francica BJ, Holtz A, Lopez J, Freund D, Chen A, Wang D, et al. Dual Blockade of EP2 and EP4 Signaling is Required for Optimal Immune Activation and Antitumor Activity Against Prostaglandin-Expressing Tumors. *Cancer Research Communications*. 2023;3:1486–500.

FIGURE LEGENDS**Figure 1. In vivo CRISPR-Cas9 screen identifies regulators of anti-tumor immunity.**

(A) Schematic of pooled CRISPR-Cas9 screen.

(B) sgRNAs targeting genes depleted *in vitro* compared to non-target controls. CRISPR score is defined as the average log₂-fold change in abundance of sgRNA reads at day 28 (in vitro) vs day 0 (in vitro) for each gene.

(C) sgRNAs targeting *Cflar* and *Zeb1* depleted *in vivo* in immune-competent and immune-deficient mice.

(D) Average log₂-fold change in abundance of sgRNA reads for all genes in immune-competent (WT) versus *Rag2*^{-/-};*Il2rg*^{-/-} mice.

(E-F) Enrichment of sgRNAs targeting *Ifngr2* (E) and depletion of sgRNAs targeting *Ptgs2* (F) in WT versus *Rag2*^{-/-};*Il2rg*^{-/-} mice. Data are mean ± SEM for (C and E-F).

(G-H) Kaplan-Meier survival of immune-competent or *Rag2*^{-/-};*Il2rg*^{-/-} mice following orthotopic transplantation with KPAR cells and *Ifngr2*^{-/-} cells (G) or *Ptgs2*^{-/-} cells (H) (n=5-10 per group). Analysis of survival curves was carried out using log-rank (Mantel-Cox) test; *** P<0.001, **** P<0.0001.

Figure 2. Tumor-intrinsic COX-2 suppresses anti-tumor immunity.

(A) Kaplan-Meier survival of mice treated with 200µg anti-NK1.1 and/or 200µg anti-CD8 or corresponding isotype control (n=5-7 per group) after orthotopic transplantation of *Ptgs2*^{-/-} cells. Treatment was initiated 3 days before transplantation and was administered once weekly until endpoint.

Analysis of survival curves was carried out using log-rank (Mantel-Cox) test; * P<0.05, ** P<0.01.

(B) Frequency of tumor-infiltrating T cell populations and NK cells in KPAR and *Ptgs2*^{-/-} orthotopic tumors.

(C) Quantification and representative immunohistochemistry staining for NKp46⁺ NK cells. Scale bar represents 100µm.

(D) Stacked bar plots showing frequency of central memory (T_{cm} – CD44⁺CD62L⁺), effector memory (T_{em} – CD44⁺CD62L⁻) and naïve (CD44⁻CD62L⁺) CD8⁺ (left) and CD4⁺ (right) T cells.

(E) Surface expression (mean fluorescence intensity) of CD44 on CD8⁺ (left) and CD4⁺ (right) T cells.

(F) Surface expression (mean fluorescence intensity) of CD86 (left) and MHC-II (right) on CD11b⁺ macrophages and CD11c⁺ macrophages.

(G) Percentage of Arg1⁺ CD11b⁺ macrophages.

(H) Quantification and representative immunohistochemistry staining for the immunosuppressive macrophage marker Arg1. Scale bar represents 100µm.

(I) Representative flow cytometry plots of CD206 and MHC-II surface expression on CD11b⁺ macrophages (left) and quantification of M1/M2 ratio based on the gated populations (right).

(J) Heatmap showing hierarchical clustering of KPAR and *Ptgs2*^{-/-} tumors based on mRNA expression of anti-tumor immunity genes assessed by qPCR. Data are mean ± SEM for (B-I), n=6-9 per group. Symbols represent pooled tumors from individual mice. Statistics were calculated by paired, two-tailed Student's t-test (B-C and E-I) or two-way ANOVA, FDR 0.05 (D); * P<0.05, ** P<0.01, *** P<0.001, **** P<0.0001.

Figure 3. COX-2/PGE2 signaling hinders response to ICB in mouse and human LUAD.

(A) Kaplan-Meier survival of mice treated intraperitoneally with 200µg anti-PD-1 after orthotopic transplantation of KPAR or *Ptgs2*^{-/-} cells, n=6-8 per group. Analysis of survival curves was carried out using log-rank (Mantel-Cox) test; * P<0.05, **** P<0.0001.

(B) Quantification and representative immunohistochemistry staining of CD8⁺ T cells in KPAR or *Ptgs2*^{-/-} orthotopic tumors on day 7 after treatment with anti-PD-1 or corresponding isotype control (IgG). Scale bar represents 100µm.

(C) Percentage of CD69⁺ CD8⁺ T cells in KPAR or *Ptgs2*^{-/-} tumors treated as in (B).

(D) Frequency of PD-1⁺, LAG-3⁺ and TIM-3⁺ CD8⁺ T cells in KPAR or *Ptgs2*^{-/-} tumors treated as in (B).

(E) Heatmap showing hierarchical clustering of KPAR or *Ptgs2*^{-/-} tumors treated as in (B) based on mRNA expression of anti-tumor immunity genes assessed by qPCR.

(F) Baseline COX-2 levels in responder and non-responder ICB-treated LUAD patients.

(G) Progression-free survival of LUAD patients treated with ICB, stratified into highest and lowest quartile based on COX-2 expression.

(H) Multivariate Cox regression analysis for the indicated variables in LUAD patients following ICB treatment (CTx, chemotherapy). Error bars represent 95% confidence interval boundaries. Data are mean ± SEM for (B-D), n=5-9 per group. Statistics were calculated using two-tailed Student's t-test (F) or one-way ANOVA, FDR 0.05 (B-D); ns, not significant, * P<0.05, ** P<0.01, *** P<0.001, **** P<0.0001.

Figure 4. COX-2 inhibition enhances the efficacy of immunotherapy.

(A) Surface expression (mean fluorescence intensity) of CD86 (left) and MHC-II (right) on CD11b⁺ macrophages and CD11c⁺ macrophages in KPAR tumors treated for 7d with 30mg/kg celecoxib.

(B-D) Percentage of Arg1⁺ CD11b⁺ macrophages (B), quantification of M1/M2 macrophages (C), and frequency of CD69⁺ CD8⁺ T cells (D) in KPAR tumors treated as in (A).

(E) Kaplan-Meier survival of mice treated intraperitoneally with 200µg anti-PD-1 and/or daily oral gavage of 30mg/kg celecoxib after orthotopic transplantation of KPAR cells. Daily celecoxib treatment was initiated on day 7 and anti-PD-1 began on day 10 and was administered twice weekly for a maximum of 3 weeks. Data from two independent experiments, n=15-16 per group. Analysis of survival curves was carried out using log-rank (Mantel-Cox) test; * P<0.05, *** P<0.001, **** P<0.0001.

(F) Quantification of CD8⁺ T cells by immunohistochemistry in KPAR tumors treated for 7d with celecoxib and/or anti-PD-1.

(G) CD8⁺ T cell phenotypes in KPAR tumors treated as in (F).

(H) mRNA expression by qPCR of anti-tumor immunity genes in KPAR tumors treated as in (F). Data are mean ± SEM for (A-D and F-H), n=5-10 per group. Samples were analysed using unpaired, two-tailed Student's t-test (A-D), one-way ANOVA, FDR 0.05 (F and H) or two-way ANOVA, FDR 0.05 (G); ns, not significant, * P<0.05, ** P<0.01, *** P<0.001.

Figure 5. Dual inhibition of EP2 and EP4 synergises with ICB.

(A-C) M1/M2 macrophage ratio (A), percentage of Arg1⁺ CD11b⁺ TAMs (B) and percentage of CD69⁺ CD8⁺ T cells (C) in KPAR tumors treated twice daily for 7d with 100mg/kg TPST-1495.

(D) Kaplan-Meier survival of mice treated intraperitoneally with 200µg anti-PD-1 and/or twice daily oral gavage of 100mg/kg TPST-1495 after orthotopic transplantation of KPAR cells, n=8-12 mice per group. TPST-1495 treatment was initiated on day 7 and anti-PD-1 began on day 10 and was administered twice weekly for a maximum of 3 weeks. Analysis of survival curves was carried out using log-rank (Mantel-Cox) test; * P<0.05, ** P<0.01, **** P<0.0001.

(E) Heatmap showing hierarchical clustering of KPAR tumors treated for 7d with TPST-1495 and/or anti-PD-1 based on mRNA expression of anti-tumor immunity genes assessed by qPCR.

(F) mRNA expression by qPCR of immune-related genes in KPAR tumors treated as in (E). Data are mean ± SEM for (A-C) and (F), n=7-8 mice per group. Statistics were calculated using unpaired, two-tailed Student's t-test (A-C) or one-way ANOVA, FDR 0.05 (F); ns, not significant, * P<0.05, ** P<0.01, *** P<0.001, **** P<0.0001.

Figure 6. Oncogenic KRAS drives immunosuppressive COX-2 expression in LUAD.

(A) Immunoblot for COX-2 (left) and ELISA analysis for PGE₂ concentration (right) in KPAR cells treated with 10nM trametinib (MEKi) for 24h or 48h.

(B-C) Immunoblot for COX-2 (B) and ELISA analysis for PGE₂ concentration (C) in KRAS^{G12C} mouse cancer cell lines treated with 100nM MRTX849 for 24h or 48h.

(D) COX-2 mRNA expression in 3LL ΔNRAS and KPAR^{G12C} orthotopic tumors treated for 7d with 50mg/kg MRTX849.

(E) COX-2-associated inflammatory signature (COX-IS) assessed by qPCR in 3LL ΔNRAS and KPAR^{G12C} orthotopic tumors treated as in (D).

(F) Immunoblot for COX-2 in human KRAS^{G12C} lung cancer cell lines treated with MRTX849 for 24h. A549 (KRAS^{G12S}) cells were used as a negative control.

(G) COX-2 expression in RAS-low and RAS-high human lung cancer cell lines from the CCLE database.

(H) COX-IS in LUAD samples from TCGA stratified by RAS-activity into five different groups which are associated with specific co-occurring mutations (RAG-1, *KRAS/LKB1*; RAG-2, *KRAS*; RAG-3, *KRAS/TP53*; RAG-4, *KRAS/CDKN2A*).

(I) Immunoblot for COX-2 in KPAR^{G12C} cells treated for 2d, 3d or 5d with 100nM MRTX849.

(J) COX-2 mRNA expression in MRTX849 on-treatment and relapsed KPAR^{G12C} tumors.

(K) Kaplan-Meier survival of mice treated with daily oral gavage of 50mg/kg MRTX849 alone or in combination with 30mg/kg celecoxib, n=8-20 per group. Analysis of survival curves was carried out using log-rank (Mantel-Cox) test; * P<0.05, **** P<0.0001. Data are mean ± SEM for (A, C-E and J), n=8-9 per group. Groups were compared using unpaired, two-tailed Student's t-test (A, C- E and G) or one-way ANOVA, FDR 0.05 (H and J); * P<0.05, ** P<0.01, ***, P<0.001, **** P<0.0001.

Figure 1

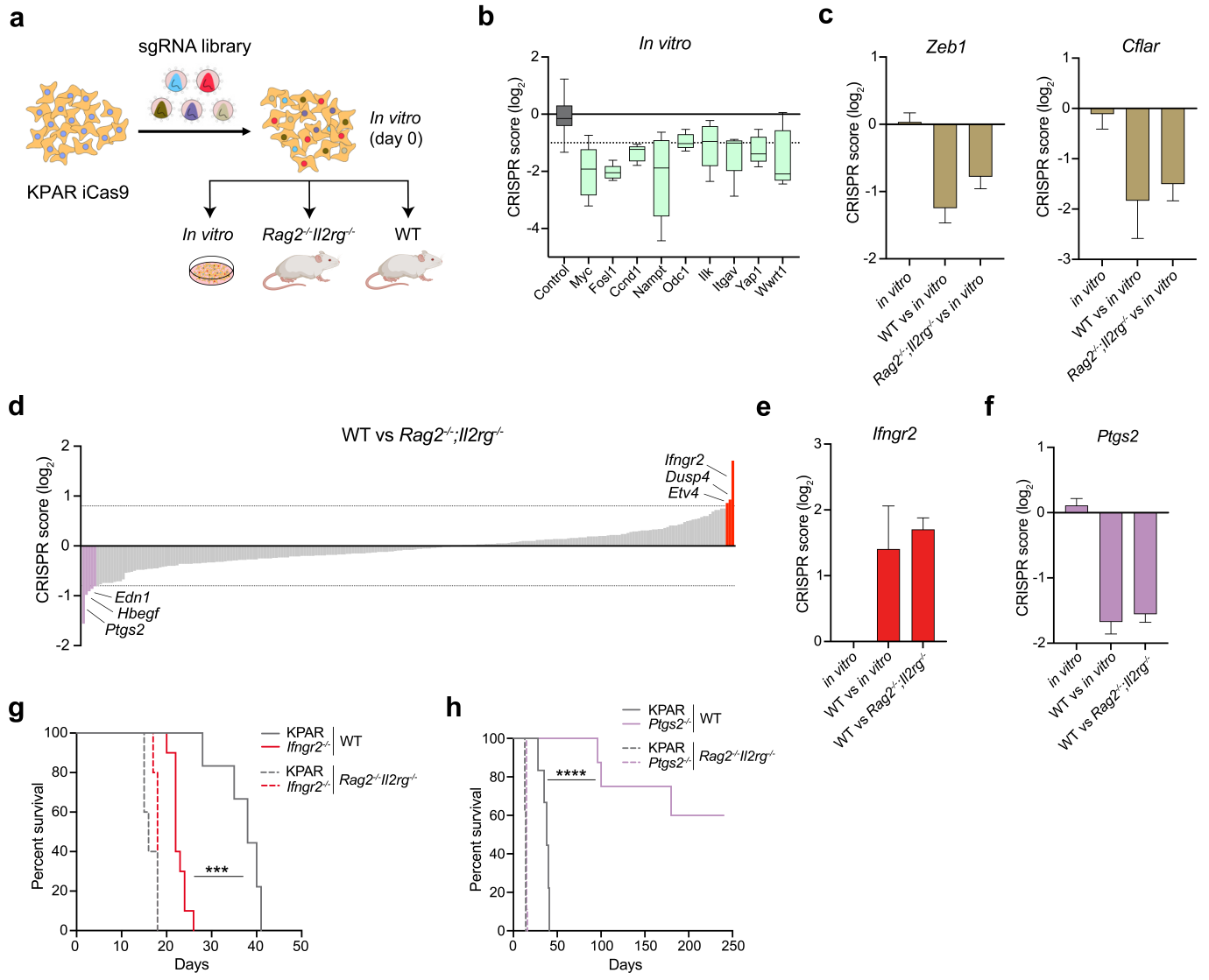


Figure 2

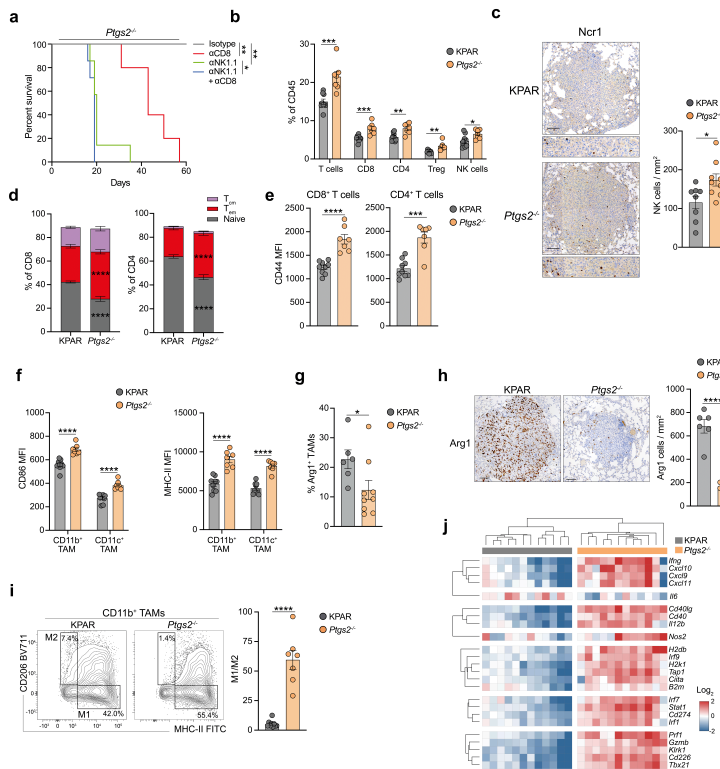


Figure 3

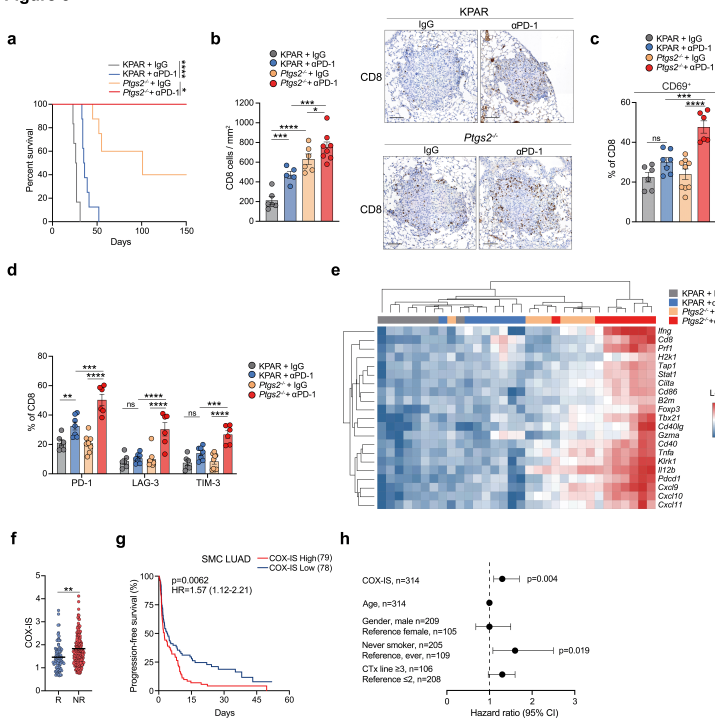


Figure 4

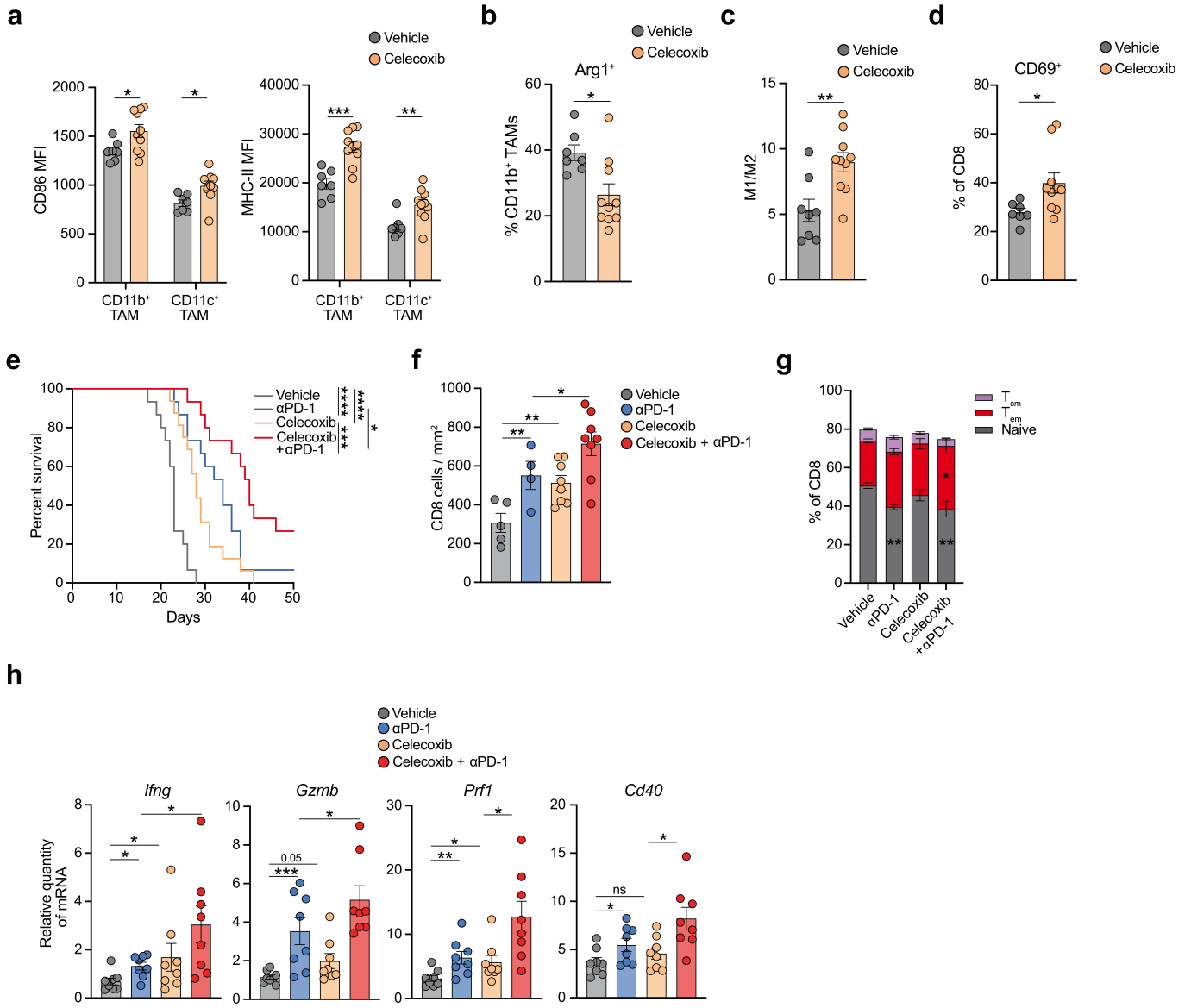


Figure 5

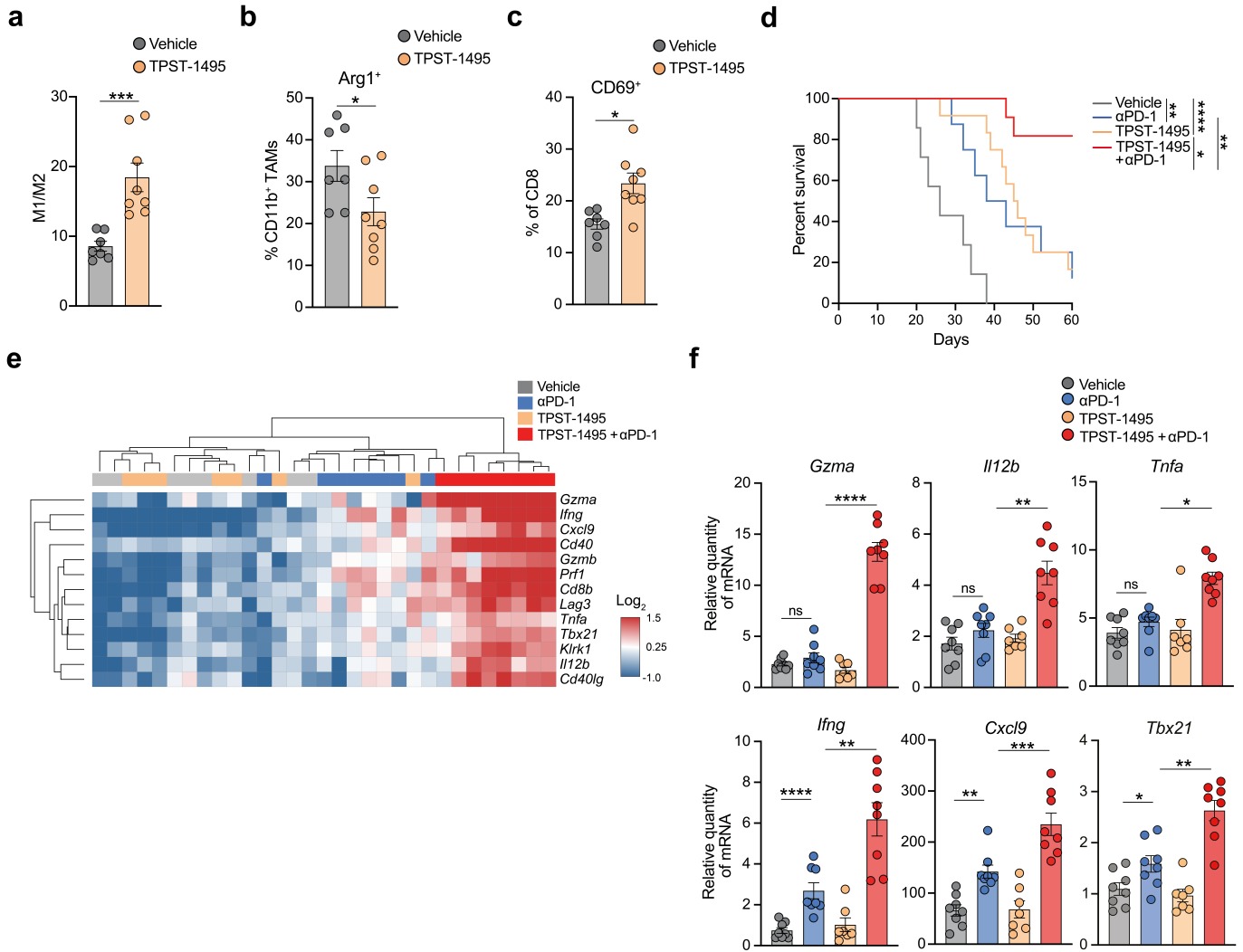
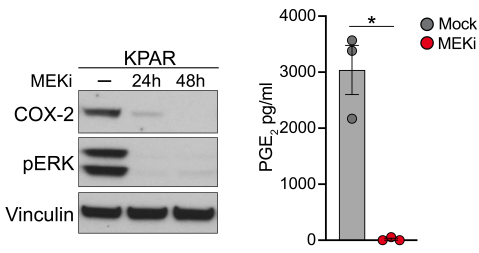
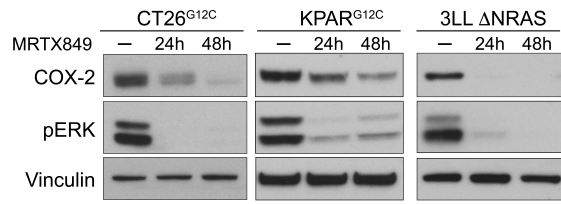


Figure 6

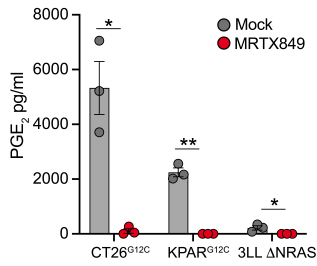
a



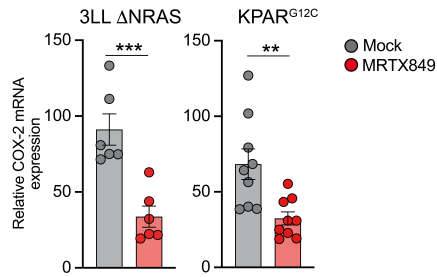
b



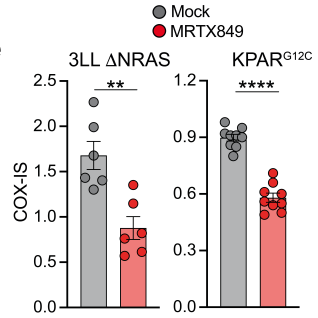
c



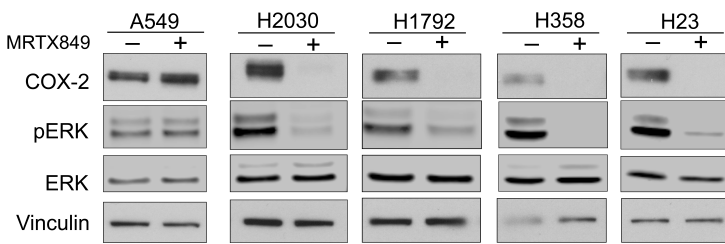
d



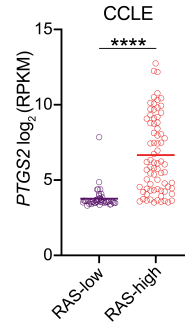
e



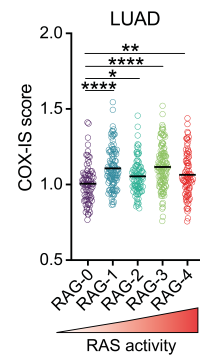
f



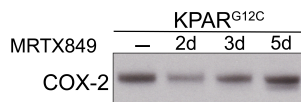
g



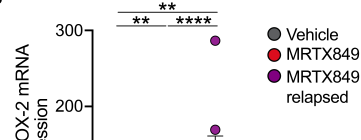
h



i



j



k

